Ligand Driven Control and F-Doping of Surface Characteristics in FASnI_3 Lead-Free Perovskites: Relation Between Molecular Dipoles, Surface Dipoles, Work Function Shifts, and Surface Strain

Pooja Basera, Boubacar Traore, Pingping Jiang, Laurent Pedesseau, Mikaël Kepenekian, Jacky Even, Claudine Katan

ADVANCED MATERIALS INTERFACES
Open Access
www.advmatinterfaces.de

Ligand Driven Control and F-Doping of Surface Characteristics in $FASnI_3$ Lead-Free Perovskites: Relation Between Molecular Dipoles, Surface Dipoles, Work Function Shifts, and Surface Strain

Pooja Basera, Boubacar Traore, Pingping Jiang, Laurent Pedesseau, Mikaël Kepenekian, Jacky Even, and Claudine Katan**

The performance and operational stability of perovskite-based devices heavily rely on the interfacial properties between the photoactive perovskite layer and charge transport layers. Understanding the theoretical relationship between surface/interface dipoles and surface energetics is crucial for scientific understanding and practical applications. In this study, a method is applied that bridges classical electromagnetism and modern atomistic approaches. The impact of dipolar ligand molecules functionalizing the $FASnI_3$ perovskite surface is investigated, with inspection of the interplay between surface dipole, charge transfer, and local strain effect, and corresponding shifts in the valence level. The results reveal that the contribution of individual molecular entities to surface dipoles and electric susceptibilities follows an essentially additive behavior. The influence of F doping usually used to mitigate Sn oxidation in Sn-based layer for photovoltaic applications, is also discussed. Furthermore, the findings are compared with predictions from classical approaches employing a capacitor model that links the induced vacuum level shift and the molecular dipole moment. The insights gained from the study provide theoretical guidelines for fine-tuning the work functions of materials, thus enabling effective interfacial engineering in this class of semiconductors.

1. Introduction

In recent years, organic–inorganic hybrid halide perovskite solar cells (PSCs) have garnered significant attention and achieved a remarkably high power conversion efficiency (PCE) of 26.15%, thanks to the dual site binding ligands that improved the charge extraction in single junction PSCs.[1] However, the toxicity and instability associated with lead (Pb)-based PSCs remain an issue that hinder their large-scale application. Significant amount of research has been devoted to replacing Pb in halide perovskites with tin (Sn), germanium (Ge), silver (Ag), bismuth (Bi), antimony (Sb), and copper (Cu).[2–8] Among these low toxicity candidates, Sn has emerged as the most successful and widely adopted strategy to reduce the bandgap (E_g) of perovskite materials, lowering it from 1.5– 1.6 to 1.2–1.4 eV.[9–12] At present, Sn-based solar cell contribute to a remarkable powePCE surge from 7.18% to 14.81%, setting a new certified record at 14.03%.[13–16]

$FASnI_3$ also holds immense potential across various other fronts, including light emitting diodes, photocatalysts, and diverse photodetector applications.[17–20] This also involves memristors, transistors, lasers, as well as diverse sensor types.[21] Additionally, $FASnI_3$ can be synthesized in various forms, including single crystals,[22] thin films,[22] nanoplatelets,[23] Sn(IV) free colloidal nanocrystals,[24] quantum dots,[25] and superlattices[26] and stabilized thanks to various ligands and may even incorporate biomolecules.[27,28]

Despite their favorable bandgap, Sn-based perovskites still face challenges in achieving high PCEs. By delving into the fundamentals of electronic structure, photophysics, and degradation pathways, the intrinsic challenges in Sn-based perovskite emerge at both the materials and device levels: i) easy oxidation of Sn^{2+} to Sn^{4+} on the surface of Sn-based perovskite thin films, ii) oxidation-induced p-type self-doping,[29] which cause severe mono-molecular recombination and bandgap widening, iii) mismatched band alignment between the active layer and the widely

P. Basera, B. Traore, P. Jiang, M. Kepenekian, C. Katan
ENSCR
CNRS
ISCR-UMR 6226
Univ Rennes
RennesF-35000, France
E-mail: claudine.katan@univ-rennes1.fr
P. Basera, P. Jiang, L. Pedesseau, J. Even
INSA Rennes
CNRS
Institut FOTON-UMR 6082
Univ Rennes
RennesF-3500, France
E-mail: Jacky.Even@insa-rennes.fr

The ORCID identification number(s) for the author(s) of this article can be found under https://doi.org/10.1002/admi.202400201

DOI: 10.1002/admi.202400201

used PEDOT:PSS hole transport layer, which hinders the collection of free carriers,[30] results in non-ideal electrical contacts and additional potential losses, iv) rapid and uncontrollable crystallization, which present a critical technical challenge toward high quality preparation of Sn-based perovskite thin films.[31] These challenges impose significant limitations on the attainable PCEs of Sn-containing perovskite-based solar cells, driving a keen interest in developing strategies to efficiently modify material energy levels.

Surface passivation and/or functionalization, including the combination of 2D and 3D perovskites has demonstrated success in finely adjusting the energy level alignments between different materials within a device.[32–35] It directly influences the surface dipoles between adjacent layers in a device stack, which in turn change materials' energetics such as its work function. Although, the influence of surface functionalization on the change of work function or valence energies is, in general, clear from experiments, the connection between them from a theoretical perspective is often not fully understood. Therefore, this motivates the need for an atomistic description of perovskite surfaces, interfaces and nanostructures, which is able to afford the link between surface dipoles and energetics and provide at the same time a support for experimental studies.

Surface functionalizations are extensively explored experimentally for metal halide perovskites. Polyatomic pseudohalides, such as thiocynate (SCN^-) and azide (N_3^-) have been effectively employed as viable alternatives to X-site halides in organic–inorganic hybrid lead-based perovskites.[2,36–41] For instance, a 2D organic–inorganic hybrid compound, $(CH_3NH_3)_2Sn(SCN)_2Cl_2$, has recently been reported.[42] Ligands such as 4-fluorophenethylammonium bromide (FPEABr), played a crucial role in forming a 2D/3D microstructure in $FASnI_3$ PSCs,[13] and were also employed to control the crystallization and mitigate the Sn^{2+}oxidation.[43] Phenylethylamine (PEA) based molecules were also introduced as the synthetic ligand and for post synthetic ligand exchange in $CsPbX_3$ (X = Br or I) quantum dots (QDs) chemistry.[44] The addition of Piperazine effectively suppressed self-doping in $CsSnI_3$ perovskite solar cells.[45–47] Substituted thiourea neutral ligands have recently been used to slow down the crystallization of $FASnI_3$ and inhibit surface defects, leading to improved film morphology.[14,31] Thiosemicarbazide (TSC) with S=C– N functional group successfully modulated defect density at surfaces and grain boundaries in $CsSnI_3$ perovskites.[48] Furthermore, the pretreatment of $FASnI_3$ perovskite film by spin coating a solution of organic halide salt n-propylammonium iodide induced templated growth of $FASnI_3$ crystals, resulting in a highly crystallized film and suppressed trap density.[49] Liquid formic acid was introduced as a reducing and volatile solvent in the $FASnI_3$ perovskite precursor solution, and also served as an anti-oxidation additive for $FASnI_3$ PSCs.[50,51] Additionally, treating the $FASnI_3$ surface with carboxylic acids and large ammonium-substituted ligands has also been implemented to modify interfacial energetics.[52] In literature, related theoretical reports for Sn based perovskites are scarce, with for instance $\gamma - CsSnI_3$ surface passivation with phenylethylammonium (PEA^+) and its halogen (X) derivatives ($XPEA^+$).[53] Therefore, there is an interest in providing comparative studies on the effect of various ligands, with variable surface coverage, on the tin-based perovskite surface/interface energetics with atomic-scale insight.

This work presents a theoretical study on $FASnI_3$ functionalized surfaces with various molecular species, based on a general theoretical framework recently developed by some of us, which bridges classical electromagnetism and modern atomistic approaches.[54,55] Investigated ligands are tetramethylthiourea (TMTU), thiosemicarbazyde (TSC), dimethylethylenethiourea (DMETU), dimethylthioacetamide (DMTA), formate anion, 4-fluoro-phenylethylammonium cation (4-FPEA), thiocynate anion (SCN), Phenylethylammonium (PEA) and n-propylammonium (PA) cations. The selection of these ligands is based on their experimental interest and relevance to the field of surface chemistry and surface modification of perovskites materials and nanocrystals, frequently serving as capping ligands or passivating agents, and crucially, for their role in tuning the interfacial energetics (vide supra). We investigate the influence of each specific ligand on the work function and delve into the microscopic origin of the induced changes in terms of surface and interface dipoles. We also study the impact of surface coverage and discuss the additivity of surface and interface dipoles as well as electric susceptibilities. Additionally, we compare our results to those predicted using the conventional empirical approach based on a capacitor model and highlight its validity within the domain of halide perovskites.

2. Results and Discussion

2.1. Ligands Under Consideration and Surface Model

Figure 1 gathers the molecules examined in this study. These include: tetramethylthiourea (TMTU, $C_5H_{12}N_2S$), thiosemicarbazide (TSC, CH_5N_3S), dimethylethylenethiourea (DMETU, $C_5H_{10}N_2S$), dimethylthioacetamide (DMTA, C_4H_9NS), formic acid (HCOOH), 4-fluoro-phenylethanamine ($C_8H_{10}FN$), thiocyanic acid (HSCN), phenylethylamine ($C_8H_{11}N$) and propylamine (C_3H_9N). Note that for formic acid and thiocyanic acid, we consider their conjugate base forms: formate anion ($HCOO^-$) and thiocyanate anion (SCN^-),[42] respectively. For 4-fluorophenylethanamine, phenylethylamine and propylamine, the corresponding conjugate acids are 4-fluoro-phenethylammonium (4-FPEA, $C_8H_{11}FN^+$), phenethylammonium (PEA, $C_8H_{12}N^+$) and propylammonium (PA, $C_3H_{10}N^+$) cations, respectively. For the sake of simplicity, we refer to the considered molecules as TMTU, TSC, DMETU, DMTA, formate, 4-FPEA, SCN, PEA and PA. Collectively, these nine ligands allow us to explore a variety of molecules including neutral as well as charged ones, with varying dipolar strength, size, orientation and interaction (electrostatic, ionic/covalent) on the perovskite surfaces. This set allows to get insights from atomistic simulations, about the interplay between surface dipole, charge transfer, and local strain effect and their impact on the valence energies. The distribution of charges in the molecules is shown via Hirshfeld charge analysis, where red (blue) indicates negative (positive) charge (Figure 1). Dipole moments from negative (red) to positive (blue) charge are denoted. Comparison of dipole moments of the optimized molecular structures with existing experimental/theoretical data is provided in **Table 1**.

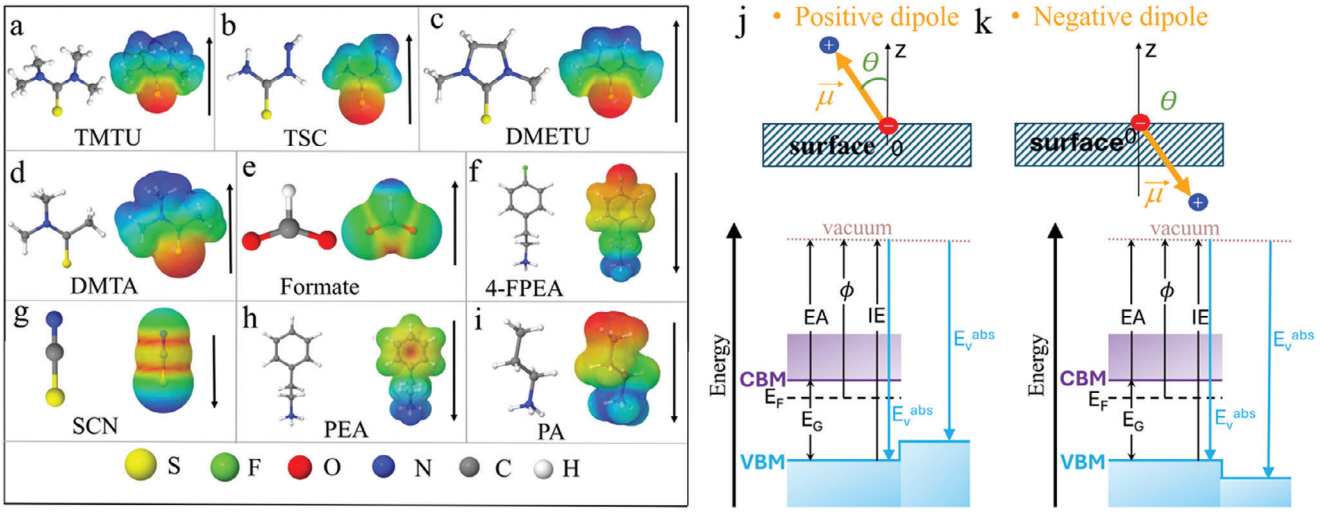

Figure 1. Molecules and their Hirshfeld charge analysis to show the direction of the dipole moment a) TMTU b) TSC c) DMETU d) DMTA e) Formate f) 4-FPEA g) SCN h) PEA i) PA. The red (blue) region indicates an excess of electronic charge (electron deficiency). The direction of the dipole moments is illustrated by black arrows. Representation of the effect of the presence of a surface dipole. Convention used for j) positive and k) negative dipoles: positive dipole moment direction is from negative to positive charge (top panel). Schematic illustration of the energy diagram of a semiconductor with band edges (VBM and CBM) and corresponding energies, fundamental energy gap (E_G), Fermi level (E_F), vacuum level, work function (ϕ), ionization energy (IE) and electron affinity (EA). The valence energy (E_v^{abs}) is defined on an absolute scale, i.e., with respect to the vacuum level. The work function (ϕ) is defined with respect to the Fermi level. In our DFT calculation free of defects, the Fermi level lies at the top of the valence band and $\phi = -E_v^{abs}$.

2.2. Surface Functionalization

2.2.1. Negative Surface Dipole Variation

Previous works have established that, in the case of tin-based halide perovskites, molecules tend to functionalize the surface by coordinating with tin, which is favored by halide vacancies experimentally evidenced.[51,64] We illustrate those scenarios with the neutral and anion ligands thiourea and formate, that have been shown to improve the crystallization kinetics and the film morphology of $FASnI_3$.[31,51] We adopt the modeling strategy from Ref., [31,48] by substituting an iodine (I) atom (outer terminal) by a sulfur atom of the TMTU, TSC, DMETU, DMTA. In doing so, we remove a neighbouring FA^* to keep the charge neutrality of the system. For formate anion, we replace the (I) atom with the oxygen (O) atom.[51] Here, we present TMTU as a case study, with the remaining ligands illustrated in more details in Sections SV and SVI, Supporting Information).

To analyze the valence energy of the pristine FA^*SnI_3 slab, we compute the Hartree potential profile (Section SII, Supporting Information). We observe a successive increase in the valence energies (E_v^{abs}) with an increase in molecular coverage (**Figure 2b**). Corresponding values are summarized in **Table 2**. To understand the origin of the shifts, we compute polarization density profiles ($P_b(z)$, Figure 2c), and analyze surface and interface dipoles.

The increase of E_v^{abs} with increased TMTU coverage (Figure 2) is ascribed to the decrease in surface dipole density (p) induced by surface functionalization. This decrease results from electron transfer from the TMTU to the outer perovskite layer, leading to a dipole direction away from the surface (Figure 2d). We delve deeper into this phenomenon by examining the interplay of octahedral tilting in the surface layer and the contraction or expansion of SnI bond lengths at the surface (see Section SIV, Supporting Information). Table S1 (Supporting Information) reveals that at 25% concentration, compared to 50% concentration, surface layers exhibit greater distortion with reduced in-plane Sn–I–Sn angles and increased out-of-plane delta (δ) octahedral tilting.[65] Notably, octahedral tilting substantially affects electronic properties,[65–67] and deviations from 180° in Sn–I–Sn bond angles lead to deeper valence levels. This indicates surface relaxation also influences surface dipole density, subsequently affecting valence energy. Given the above, altering TMTU surface coverage finely adjusts work function by several meV, causing valence levels to rise as coverage increases. As a general guidance for experimentalists, it means that besides intrinsic dipolar properties of the molecules attached to the surface, local investigations related to surface strain might be interesting to have a better insight into the band alignments in a heterostructure. It is already known that using grazing incidence X-Ray diffraction or

Table 1. Computed molecular dipole moments (PBE), and values from the literature, where subscripts e and t denote experimental and theoretical reported values.

Molecules	μ (D) (this work)	μ (D) (previous works)
TMTU	4.18	4.70_e[56]
TSC	5.18	4.05_t[57]
DMETU	4.58	4.09_e[58]
DMTA	5.24	4.74_e,[59] 5.51_t[59]
Formic acid	1.47	1.41_e[60]
4-fluoro-phenylethanamine	2.34	2.02_t[43]
Thiocyanic acid	3.64	3.50_t[61]
Phenylethylamine	1.38	1.26_t[62]
Propylamine	1.53	$1.20 - 2.0_e$[63]

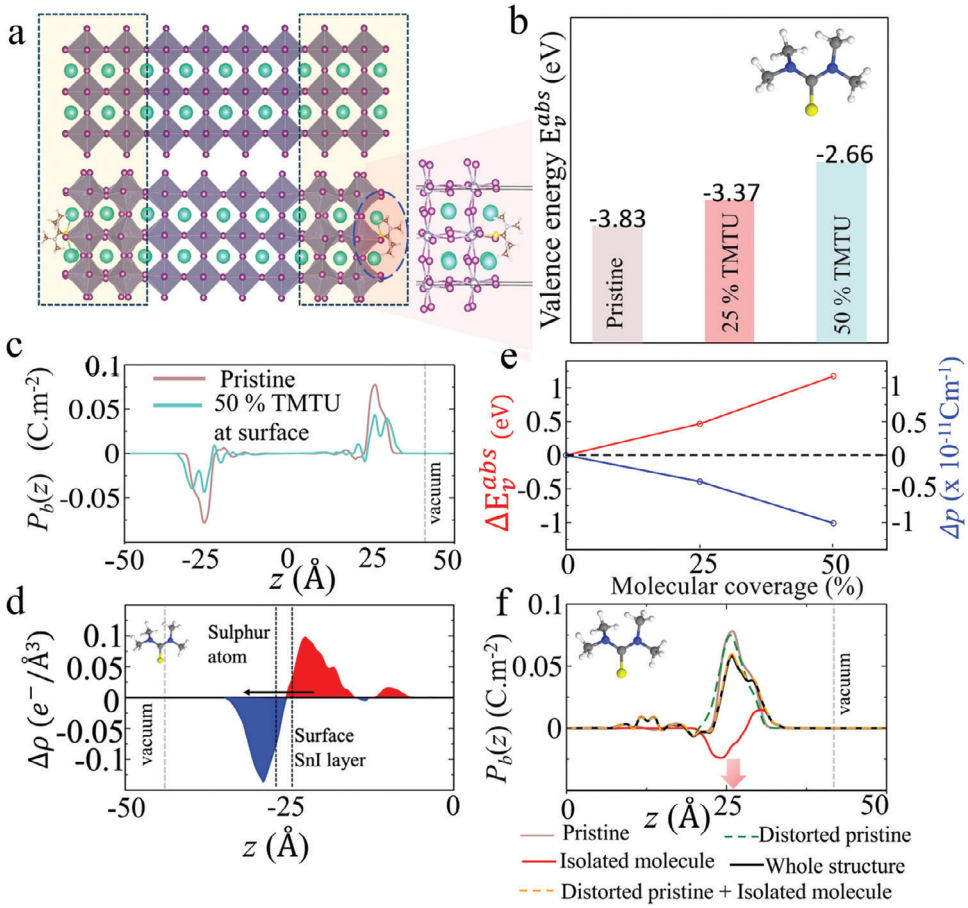

Figure 2. a) FA*SnI$_3$ FA*I terminated slabs without (top) and with (bottom) TMTU ligands attached to the surface. The latter case is shown for a 25% molecular coverage. b) Valence energies for 0% to 50% surface coverage. Valence energy values are determined from the Hartree potential profiles. c) Polarization density profiles for 0% and 50% molecular coverage. The integration of these polarization profiles results in the surface dipole densities (Table 2). d) Variation of the electronic charge density upon TMTU functionalization at 25% molecular coverage. For clarity, only one side of the symmetric slab is displayed. Red and blue color indicate electronic accumulation and depletion region, respectively, while the arrow denotes the net dipole direction. e) Relation between the change in the valence energies and the surface dipole density with respect to molecular coverage. f) Illustration of the additive nature of surface dipole densities via polarization density profiles (P_b(z)).

Ultraviolet Photoelectron Spectroscopy (UPS)/X-Ray Photoelectron Spectroscopy (XPS) among others might be useful from that perspective.[68,69]

Next, we expand to discuss other molecules TSC, DMETU, DMTA, and formate anion.[14,31] Table 2 lists E_v^{abs} and surface dipole density values for different concentrations. Upward valence shifts observed for TSC, DMETU, DMTA and formate anion are driven by reduced surface dipole density due to molecule-to-outer-perovskite charge transfer (Sections SV and SVI, Supporting Information). The upward shift in valence levels for formate anion in FA*SnI$_3$ surface is in agreement with recent experimental findings.[51] At different surface coverages, Δp and ΔE_v^{abs} for TMTU vary linearly with molecular coverage (Figure 2e,f). Notably, Hartree potential alignment computed ΔE_v^{abs} is in excellent agreement with ΔE_v^{abs} calculated using Equation 3 (Table 2). To summarize, all studied cases show an upward valence level shift as surface coverage increases. The observed trend in effectively tuning the E_v^{abs} energies is DMETU > TMTU > DMTA > TSC > formate anion. Additionally, these molecules hold promise as passivating agents, as they do not introduce any molecular states between their perovskite-based band edges (Figure S12, Supporting Information).

From our investigation of different ligands on the FA*SnI$_3$ surface, resulting in negative surface dipole density variations, the increase in the valence energies appears directly linked to the dipole density of the individual components comprising the whole structure. Hence, it is interesting to disentangle the individual role of each effects at the interface. We do so for the example of TMTU molecules on a FA*I terminated FA*SnI$_3$ surface. Figure 2f shows the polarization density profiles (P_b(z)) computed for i) the pristine perovskite (FA*I slab), ii) the distorted pristine, where the outer layer experiences the distortion caused by FA* vacancies, iii) an isolated molecule, and iv) the whole structure. The addition of P_b(z) profiles from the distorted pristine and the isolated molecule replicates the P_b(z) profile of the whole structure. From these P_b(z) profiles, we observe that at the interface, the TMTU molecule counteracts the polarization density of pristine perovskite. This results in a net reduction of the surface dipole density, subsequently lowering the work function and leading to an upward shift of the valence level.

Table 2. Valence energies (E_v^{abs}) and surface dipole densities (p) calculated at the PBE+SOC level for various molecules and molecular coverages, ranging from 0% to 75% on FA*I-terminated FA*SnI_3 slabs. Change in surface dipole densities (Δp). Shifts in valence levels ΔE_v^{abs} determined by the Hartree potential alignment [HP] or using the difference of surface dipole density (Equation 3).

	E_v^{abs}[eV]	ΔE_v^{abs} [HP] [eV]	$p \times 10^{-11}$ [C/m]	$\Delta p \times 10^{-11}$[C/m]	ΔE_v^{abs} [Equation 3] [eV]
FA*SnI_3 pristine slab					
0%	− 3.83	–	+3.72	–	–
FA*SnI_3 slab with TMTU					
25%	− 3.37	+0.46	+3.32	− 0.40	+0.45
50%	− 2.66	+1.17	+2.70	− 1.02	+1.15
FA*SnI_3 slab with TSC					
25%	− 3.43	+0.40	+3.38	− 0.34	+0.38
50%	− 3.20	+0.63	+3.17	− 0.55	+0.62
FA*SnI_3 slab with DMETU					
25%	− 3.28	+0.55	+3.25	− 0.47	+0.53
FA*SnI_3 slab with DMTA					
25%	− 3.41	+0.42	+3.36	− 0.36	+0.41
50%	− 3.09	+0.74	+3.08	− 0.64	+0.72
FA*SnI_3 slab with formate					
25%	− 3.70	+0.13	+3.61	− 0.11	+0.12
50%	− 3.47	+0.36	+3.40	− 0.32	+0.36
75%	− 3.33	+0.50	+3.28	− 0.44	+0.49

2.2.2. Positive Surface Dipole Variation

NH_4SCN is widely used to regulate the structure of a 2D-quasi-2D-3D Sn perovskite film.[2,38] Experimental UPS analysis of varying SCN amounts (0 to 15%) demonstrates a downward shift in the valence levels.[2] The same E_v^{abs} decrease is observed in bulk 3D tin perovskites upon SCN anion inclusion (FA*$SnI_{3-x}(SCN)_x$, x = 0, 1, 2, and 3).[36] In light of the available experimental data, we compute the valence energies and surface dipole densities as a function of molecular coverage for the SCN anion on FA*SnI_3 surface. Considering the reported crystal structures for adducts between SCN and metals such as Pb or Sn,[42,70] an iodine atom is replaced by the sulfur of the SCN anion. The relaxed structure of the slab with SCN anions is shown in **Figure 3a** (middle panel). We observe a gradual decrease in E_v^{abs} with an increase in SCN anion coverage ranging from 0 to 100% (Figure 3b, top panel).

Recently, fluorination has emerged as a potent strategy to enhance both organic and perovskite solar cell performance, promoting exciton dissociation and charge transport by introducing a strong electric dipole moment through fluorine substitution on PEA cations.[71–74] The high electronegativity of fluorine atom withdraws electrons, causing NH_3^+ cations to accumulate more positive charge, resulting in a stronger electrostatic interaction between ligand and the $[SnI_6]^{4-}$ framework.[75] The NH_3^+ group of $FPEA^+$ cation substitutes a FA*-atom of the outer layer of the FA*SnI_3 surface Figure 3a (bottom panel). We note a downward shift in valence levels for molecular coverage varying from 25 to 100% (Figure 3b, bottom panel). The linear correlation persists for both ΔE_v^{abs} and Δp as molecular coverage increases for both the FPEA cation and SCN anion (Figure S14, Supporting Information). Figure 3c illustrates the additive nature of surface dipoles using FPEA as an example. From the profile, we notice at the interface, the FPEA molecule largely align in the same direction as the pristine perovskite, resulting in a substantial increase in the surface dipole density and the decrease in valence energy. The decrease of E_v^{abs} for FPEA cation is attributed to the increase in surface dipole density induced by surface functionalization (**Table 3**). Notably, a 2D tin-perovskite capping layer with FPEA cations provides protection for 3D $FASnI_3$ grains, yielding a remarkable PCE of 14.81%.[8]

Recently, P. Li et al. have reported FPEA derivatives that improved the crystallinity of the perovskite films and monitor the energy level alignments with UPS measurements at low (8%) concentration.[43] Inspired by this work, we perform a comparative analysis of three isomeric fluorinated ligands (4-FPEA, 3-FPEA and 2-FPEA), at an approaching low concentration (11%). Such concentration is achieved by turning to an in-plane 3×3 supercell with 2 k-points in each direction (Figure 3d). At a coverage of 11%, we observe the following trend for E_v^{abs}: 2-FPEA > 3-FPEA > 4-FPEA (Figure 3e, bottom panel). The magnitude of this downward shift is directly correlated with the absolute values of the dipole moments: 4-FPEA, 3-FPEA, and 2-F-PEA exhibit dipole moments of 2.02, 1.30, and 0.90D, respectively.[43] We note a downward shift in the valence levels of 3-FPEA and 4-FPEA in comparison to the pristine energy levels, which is consistent with experimental observations. However, the overall trend does not align with the experimental data reported for the valence bands derived from UPS spectra analysis (Figure 3e (top panel)).[43] This is related to several effects not considered in our functionalized slab modeling. First, in experiments, presence of I_2 and I_3^- on the pristine surface is reported as well as a decreasing amount of Sn^{4+} with increasing number of ligands. In addition, the experiments provide substantial evidence of a notable shift in the Fermi level with respect to the vacuum, indicative of a p-doped semiconductor.[43] Hence, this example of isomeric fluorinated ligands clearly highlights the limitation of the considered

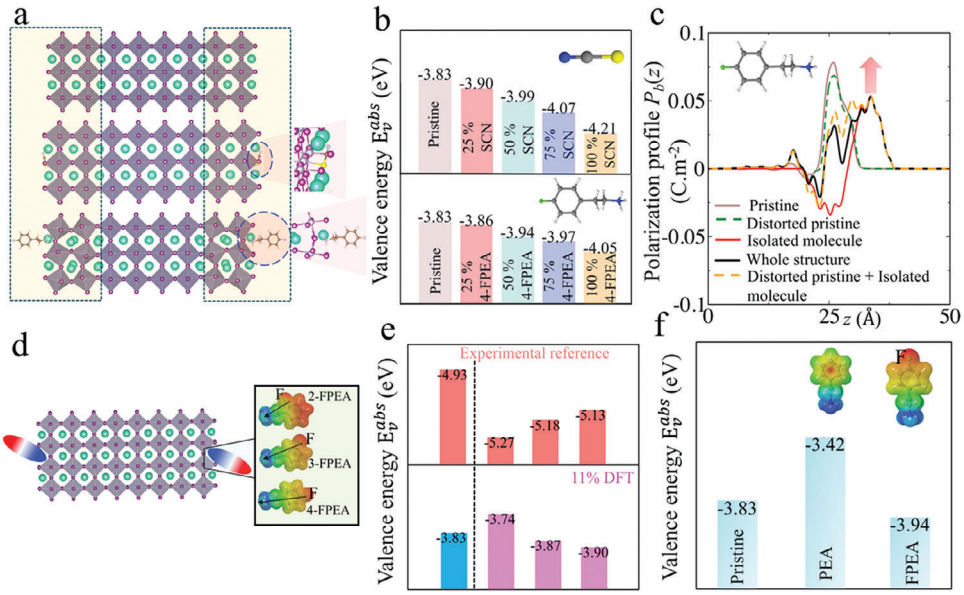

Figure 3. a) FA*SnI$_3$ FA*I terminated slabs without (top) and with (bottom) SCN and FPEA ligands attached to the surface. The NH_3^+ group is placed at a FA*-vacancy of the outer layers on each side of the surface and is illustrated with 25% molecular coverage (see zoom view). b) Valence energies computed from the Hartree potential profiles for 0% to 100% surface coverage. c) Additivity of surface dipole densities illustrated with the plot of the polarization density profiles ($P_b(z)$) computed for FPEA on a FA*I terminated FA*SnI$_3$ surface. For clarity, only one side of the symmetric slab is shown. d) FA*SnI$_3$ FA*I terminated slabs with FPEA derivatives (2-FPEA, 3-FPEA and 4-FPEA) ligands on the surface, and is illustrated for 11% molecular coverage. e) Experimental valence energies (top panel, red)[43] and DFT computed E_v^{abs} for 11% surface coverage (bottom panel, pink). f) Comparison of valence energies of pristine FA*SnI$_3$, FA*I terminated slab without and with PEA, and 4-FPEA cations at 50% molecular coverage. The remaining molecular coverage (25%, 75%, and 100%) of PEA cations on FA*I-terminated slab is provided in the Supporting Information. The electrostatic potential map shows a more pronounced charge separation in the FPEA cation compared to the PEA cation.

defect- and dopant-free surface models but at the same time provides insight on the sole effect of surface dipole modification.

Furthermore, experimental studies have demonstrated that the incorporation of bulky cations like PEA can improve band alignment and efficiency in mixed Sn-Pb halide perovskite solar cells,[76] also employed as an ultrathin, low-dimensional perovskite layer on the surface of FASnI$_3$ solar cells.[77] The experimentally observed upward shift in E_v^{abs},[77] aligns well with the results of our calculations as presented in the Section SVII, Table S9 (Supporting Information). Likewise, the behavior of the PA cation[49] exhibits similarities, as shown in Section SVII, Table S9 (Supporting Information). It is noteworthy that when comparing 4-FPEA and PEA cations on the FA*SnI$_3$ slab, the PEA cation exhibits an upward shift in valence levels, whereas the FPEA cation demonstrates a downward shift compared to the pristine slab (Figure 3f). This highlights the role of fluorine atoms in withdrawing electrons from the benzene ring, resulting in significant charge separation within the molecule. This, in

Table 3. Valence energies (E_v^{abs}) and surface dipole densities (p) computed at the PBE+SOC level for SCN and FPEA ligands with coverage changing from 0% to 100% on FAI-terminated FA*SnI$_3$ slabs. Change in surface dipole densities (Δp). Shifts of valence levels ΔE_v^{abs} computed from the Hartree potential alignment [HP] and from the difference of surface dipole density (Equation 3).

	E_v^{abs}[eV]	ΔE_v^{abs}[HP][eV]	$p \times 10^{-11}$ [C m^{-1}]	$\Delta p \times 10^{-11}$[C m^{-1}]	ΔE_v^{abs}[eV] [Equation 3]
FA*SnI$_3$ slab with SCN anion					
Pristine	− 3.83	–	+3.72	–	–
25%	− 3.90	− 0.07	+3.78	+0.06	− 0.06
50%	− 3.99	− 0.16	+3.86	+0.14	− 0.15
75%	− 4.07	− 0.24	+3.93	+0.21	− 0.23
100%	− 4.21	− 0.38	+4.06	+0.34	− 0.38
FA*SnI$_3$ slab with FPEA cation					
Pristine	− 3.83	-	+3.72	–	–
25%	− 3.86	− 0.03	+3.77	+0.05	− 0.05
50%	− 3.94	− 0.11	+3.85	+0.13	− 0.14
75%	− 3.97	− 0.14	+3.87	+0.15	− 0.16
100%	− 4.05	− 0.22	+3.95	+0.23	− 0.26

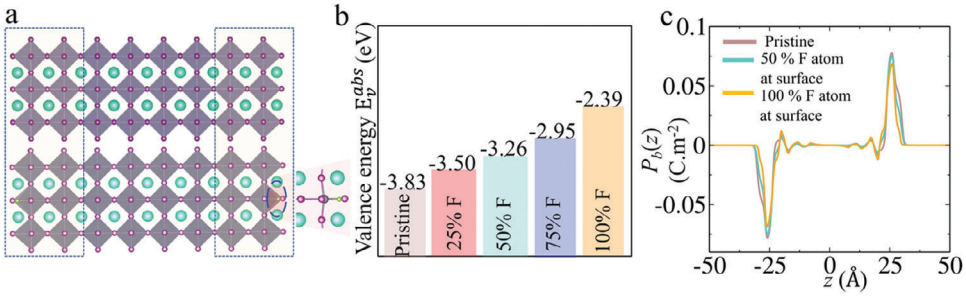

Figure 4. a) FA^*SnI_3 FA^*I terminated slabs without (top) and with F atom on the surface for a coverage of 25%. Corresponding b) valence energies and c) polarization density profiles.

turn, gives rise to a strong dipole—a characteristic not observed with the PEA cation. This trend is consistent with T. Liu's recent observation of the energy levels obtained by UPS spectra for $MAPbI_3$ films.[78]

2.3. Effect of F atom on FA^*SnI_3 slab

In order to prevent the oxidation of Sn^{2+} to Sn^{4+}, various additives such as SnF_2 have been incorporated into precursor solutions leading to enhanced perovskite film quality.[79] Gupta et al. reported a ≈0.2 eV upward shift in the band edges of $CsSnBr_3$ upon SnF_2 addition,[80] while another study also demonstrated an upward shift in valence levels with varying coverage.[81] While Nishikubo et al. found no shift in valence band edge positions for $MASnI_3$ or $FASnI_3$ with SnF_2, they did observe a slight change in the edge position upon air exposure.[82]

Considering the varying experimental reports in the literature, we revisit the role of F atom through substitution of the I atom on the FA^*SnI_3 surface (**Figure 4a**). We observe an upward shift in E_v^{abs} shown in Figure 4b (see values Table S10, Supporting Information). According to our study, the intrinsic trend is related to the change in surface dipole density obtained by integrating the area under the peak of $P_b(z)$ (Figure 4c). Our findings may offer insight into experiments, suggesting that an upward shift in the valence band edges is the most likely scenario when the FA^*SnI_3 surface is functionalized with F-atoms. This trend mirrors observations in experiments involving $CsSnBr_3$ upon the addition of SnF_2.[81] The potential huge shift of the valence band associated with the addition of SnF_2 is something that could be incorporated into the design of Sn-based perovskite cell architectures. Besides, material characterization techniques should be used to check whether this addition is leading to F accumulation at the surface.

2.4. Determination of an Effective Dielectric Surface Constant

The variation of the dielectric properties along a stack in a multilayered heterostructure are usually introduced in classical empirical modeling of optoelectronic devices by considering bulk dielectric properties of individual layers. However, in order to get an insight into interfacial contributions to the dielectric constant profile advanced first-principles methods are required.[83–85] We utilize this approach to showcase the combined effect of electric susceptibility contributions on surfaces functionalized with molecular ligands. We compute the position-dependent high-frequency dielectric profile along the stacking axis (z) for perovskite surface-attached molecule TMTU (**Figure 5**). At the center of the pristine slab, we recover a value of $\varepsilon_{r1} = 7.81$ for the dielectric constant, in good agreement with prior work.[86] The same value is obtained at the center of the slab in presence of the TMTU molecule. On the other hand, the behavior near the surface varies. By applying the following equation,[87]

$$\varepsilon_{\infty}^{\text{whole structure}}(z) = \varepsilon_{\infty}^{\text{pristine distorted}}(z) + \varepsilon_{\infty}^{\text{isolated molecule}}(z) - 1 \quad (1)$$

the dielectric constant profiles of the entire structures can be effectively decomposed into its individual components, showcasing the additive nature of electric susceptibilities. We have taken some of the molecules investigated in this study as examples; their position-dependent high-frequency dielectric profiles (ε_{r2}) are provided in the Section SXII (Supporting Information), with values ranging between 1 and 1.3. Further, we have compared ε_{r2} with ε_r calculated using the traditional capacitor model (vide infra).

2.5. Reassessing the Traditional Capacitor Model for Molecular Functionalization of Pb-free Halide Perovskite Surfaces

We revisit the conventional capacitor model,[88,89] widely applied on surfaces like Au metals[90] and TiO_2.[91] In this model, the surface's work function is modulated by − eΔV, where ΔV is the potential drop in the capacitor model, leading to $\Delta\phi = -e\Delta V$. The expression for $\Delta\phi$ is derived from Poisson's equation, as follows:

$$\Delta\phi = -e\frac{N_s \mu \cos\theta}{\varepsilon_r \varepsilon_0} \quad (2)$$

Here, N_s, μ, θ, ε_r, and ε_0 denote the number of dipoles per unit area, dipole moment, tilt angle between the dipole and surface normal (Figure 1j), dielectric constant, and permittivity of free space, respectively. Equation 2) provides valuable insights into the influence of molecular dipoles on device properties, encompassing molecular orientation and surface coverage. However, this formulation depends on the choice of dielectric permittivity, as previously discussed for monolayers at the water-air interface.[88] Two plausible values of ε_r can be considered: i) ε_{r1} for the perovskite material and ii) the effective dielectric constant ε_{r2} at the molecule positions.

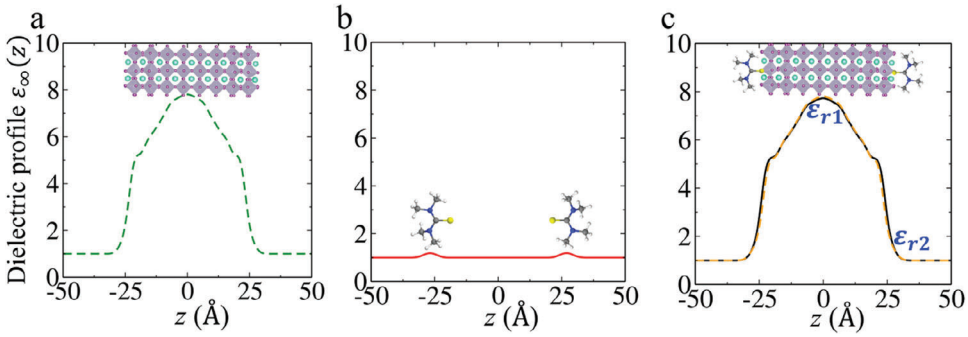

Figure 5. Additivity of electric susceptibilities illustrated with the plot of the position dependent high frequency dielectric profiles ε_∞ computed for TMTU ligand on a FA*I terminated FA*SnI_3 surface. Dielectric profile for a) distorted pristine b) isolated molecule c) whole structure (black color) and sum of distorted pristine and isolated molecule (orange color).

By combining DFT-calculated dipole moments (μ) from isolated molecules (Table 1), dipole orientations from optimized functionalized surfaces, and $\Delta\phi$ ($-\Delta E_v^{abs}$) obtained via the Hartree potential, we determine the effective dielectric constants ε_r (**Table 4**). Notably, the dielectric constant at the molecule positions closely approximates the value needed for an approximate capacitor model, but agreement is qualitative. Additionally, the dipole orientation significantly deviates from the ideal scenario where $\theta = 0$. Thus, the capacitor model shall in no case be considered as quantitative. Meanwhile, our semi-classical approach allows recovering the trends already captured by a simple capacitor model with possibly quantitative predictions, and further provides atomistic information at the interface. This insight sheds light on the interplay among surface dipoles, surface relaxation, and charge transfer, all of which directly influence the work function.

3. Conclusions and Perspectives

In summary, we used a recently developed methodology that establishes a close relationship between variations in surface dipole density and the work function, employing both classical Maxwell's equations and first-principles calculations. The key findings of this work are outlined here:

i. Quantitative prediction of valence energy level shifts with atomistic understanding: Although, the influence of surface passivation and/or functionalization on the change of work function or absolute valence energy levels is, in general, clear from experiments, the connection between them from a theoretical perspective is often not reported in a quantitative manner. Here, we show through $FASnI_3$ case systems the predictive power of the methodology, as well as its limitations, and how the shifts in valence energy levels can be interpreted in terms of surface dipoles, charge transfer and surface relaxation (lattice strain).

ii. Role of F atom on $FASnI_3$ slab: In order to prevent the oxidation of Sn^{2+} to Sn^{4+}, various additives such as SnF_2 have been incorporated into precursor solutions leading to enhanced perovskite film quality. We investigate the effects of F-doping on surface properties and work function, noting an upward shift in the valence levels.

iii. Demonstration of additivity of surface dipole densities and electric susceptibilities: Taking two examples with inverted surface dipoles, we show that surface dipole densities and electric susceptibilities are quasi-additive in functionalized surfaces, illustrating how the present methodology allows to inspect -down to the atomic scale- the interplay between surface dipoles and band edge energy levels and its potential to provide guidance for readjustment of band alignments in buried interfaces.

iv. Assessment of purely classical approaches for molecular dipoles at interfaces: Classical approaches are popular among experimentalists and sometimes theoreticians to discuss the effect of dipolar monolayers on the potential drop across interfaces. By computing the various ingredients of the well-known capacitor model from first principles, we inspect the strengths and weaknesses of the model.

v. Generality of the approach: Surfaces and interfaces are pervasive in nanostructures and devices across different

Table 4. Calculated effective dielectric constants (ε_r) using Equation 2), where $\Delta\phi$ corresponds to the work function change ($\Delta\phi = -\Delta E_v^{abs}$) determined via the Hartree potential approach. μ represents the dipole moment obtained from DFT calculations (Table 1), and θ denotes the tilt angle between the dipole and the surface normal (Figure 1j). ε_{r1} and ε_{r2} are the dielectric constants of the perovskite materials and the effective dielectric constant at the molecule position, respectively.

Molecule	$\Delta\phi = -\Delta E_v^{abs}$	μ [D]	θ (°)	$\mu\cos\theta$ [D]	$\varepsilon_r = \frac{-eN\mu\cos\theta}{\varepsilon_0\Delta\varphi}$	ε_{r1}	ε_{r2}
TMTU	− 0.47	4.18	53	2.52	1.26	7.81	1.18
TSC	− 0.40	5.18	60	2.59	1.53	7.81	1.10
DMETU	− 0.55	4.58	26	4.09	1.76	7.81	1.22
DMTA	− 0.43	5.24	53	3.15	1.74	7.81	1.15
Formic acid (formate)	− 0.13	1.47	39	1.14	2.07	7.81	1.04

technological applications. In all these systems, the properties of surfaces and interfaces play a key role. Our computational strategy provides practical means to design and optimize surface and interface energies for enhanced optoelectronic device performance, extending its applicability well beyond the specific context of metal halide perovskites.

Further extensive combined theoretical and experimental investigations are required to capture the complexity of surfaces and interfaces and we hope that the present study will stimulate work in this direction.

4. Experimental Section

Density functional theory (DFT) calculations are carried out using a finite-range numerical atomic orbital basis set within the SIESTA code.[92,93] The van der Waals density functional with C09 exchange[94] within the van der Waals DF2 (exchange-correlation term) framework was employed to optimize atomic positions.[95] In order to mimic the structural properties of 3D bulk materials at room temperature, Cs as a pseudoatom was employed instead of FA (FA^*SnI_3, FA^* = FA replaced with Cs).[54] The structures are relaxed using the fast inertial relaxation engine (FIRE) algorithm[96] until they fulfill the following relaxation criteria: i) energy difference $<10^{-4}$ eV for two consecutive ionic steps, and ii) maximum atomic forces <0.02 eV Å^{-1}. Single-point calculations are performed using generalized gradient approximation (GGA) with PBE functional,[97] accounting for spin-orbit coupling[98] over vdwDF2-C09 optimized structures. For bulk FA^*SnI_3, a polarized double-zeta basis set with a 50 meV energy shift is employed. Accurate surface property description requires diffuse orbitals (6s, 6p, 6d) for I atoms on the top two atomic layers on both sides of the slab, using 30% diffuse orbital size or cutoff radii.[99] Calculations adopt a real space mesh grid energy cutoff of 350 Ry. High-frequency dielectric constant profiles involve an electric field of 0.025 V Å^{-1} along the [001] direction. Additional computational details are provided in Section SI (Supporting Information).

Next, the methodology used to establish the relations between surface/interface dipoles and work functions was briefly outlined. A semi-classical approach combining classical physics with DFT calculations is employed as discussed in more detail in previous works.[54,55] The surface is modeled with a perovskite slab composed of layers perpendicular to the z-axis. The convention for the dipole of the molecule deposited on the surface is shown in Figure 1. The functionalization of the surface with molecules results in two types of dipoles: the intrinsic molecular dipole and the one arising from molecule-surface interactions. Both affect the perovskite surface energetics. The slab is designed to ensure the dipole density to vanish in the central bulk region ($z = z_0 = 0$), as well as in the middle of the vacuum region (at $z = \frac{c}{2}$) (see details in Section SII, Supporting Information). To bridge this approach with Leung et al.,[100] the numerical implementation of the surface dipole density $p = \int_{z_0}^{c/2} P_b(z)dz$ is combined with Poisson's equation to obtain the work function ($\phi = e\frac{p}{\varepsilon_0}$). For semiconductors, DFT calculations of defect-free surfaces at T = 0 K,[54,55] relating the work function ϕ to the energy of the top of the valence band (E_v^{abs}, with origin fixed at the vacuum level) is feasible, $E_v^{abs} = -\phi = -e\frac{p}{\varepsilon_0}$. The relationship between a shift in the valence energy (ΔE_v^{abs}) and a change in surface dipole density Δp reads:

$$\Delta E_v^{abs} = -e\frac{\Delta p}{\varepsilon_0} = -1.809 \times 10^{-8}\Delta p \quad (3)$$

In this work, the DFT-based approach was further validated by comparing ΔE_v^{abs} values obtained from Equation 3 to shifts in valence energies determined by using the well-known method of Hartree potential alignments (ΔE_v^{abs}).[101]

The robustness of the methodology was assessed by examining slab of $FASnI_3$ without functionalization of the surfaces. FA^*SnI_3 slab was constructed from its cubic structure.[102] The FA^*I terminated surface is found to be more stable than the SnI_2 terminated surface during crystal growth,[103] thus, focus on the FA^*I terminated (001) surface of FA^*SnI_3. Specifically, a slab with a thickness of 8 octahedra layers and a 2×2 in-plane supercell was considered to investigate the impact of surface functionalization (see Supporting Information for details). Charge density, polarization density profiles, surface dipole densities, and Hartree potential alignments (Figure S1, Supporting Information) are used to compare different approaches to compute work function shifts. Notably, the limitations of the used PBE functional were acknowledged in accurately predicting band edge energy levels as well as bandgaps in certain cases. Expanding beyond the PBE level, such as with hybrid functionals or GW, particularly for systems with thousands of atoms, is impractical. Therefore, in addition to the valence energies E_v^{abs}, surface dipole shifts Δp and work function shifts ΔE_v^{abs} (Tables 2 and 3) were also provided. Remarkably, these shifts remain generally well determined regardless of whether PBE or higher-level theories are employed.

Supporting Information

Supporting Information is available from the Wiley Online Library or from the author.

Acknowledgements

Authors acknowledge funding from the European Union's Horizon 2020 program, through an Innovation Action under grant agreement No. 861985 (PeroCUBE) and through a FET Open research and innovation action under the grant agreement No. 899141 (PoLLoC). J.E. acknowledges the financial support from the Institut Universitaire de France. This work was granted access to the HPC resources of TGCC under the allocations 2021-A0110907682 and 2022-A0110907682 made by GENCI.

Conflict of Interest

The authors declare no conflict of interest.

Author Contributions

The manuscript was written through contributions of all authors. All authors have given approval to the final version of the manuscript.

Data Availability Statement

The data that support the findings of this study are available from the corresponding author upon reasonable request.

Keywords

interface, Pb-free perovskites, surface, work function

Received: March 3, 2024
Revised: May 17, 2024
Published online:

[1] H. Chen, C. Liu, J. Xu, A. Maxwell, W. Zhou, Y. Yang, Q. Zhou, A. S. R. Bati, H. Wan, Z. Wang, L. Zeng, J. Wang, P. Serles, Y. Liu, S. Teale, Y. Liu, M. I. Saidaminov, M. Li, N. Rolston, S. Hoogland, T. Filleter, M. G. Kanatzidis, B. Chen, Z. Ning, E. H. Sargent, *Science* **2024**, *384*, 189.

[2] F. Wang, X. Jiang, H. Chen, Y. Shang, H. Liu, J. Wei, W. Zhou, H. He, W. Liu, *Joule* **2018**, *2*, 2732.
[3] F. Hao, C. C. Stoumpos, P. Guo, N. Zhou, T. J. Marks, R. P. H. Chang, M. G. Kanatzidis, *J. Am. Chem. Soc.* **2015**, *137*, 11445.
[4] T. Krishnamoorthy, H. Ding, C. Yan, W. L. Leong, T. Baikie, Z. Zhang, M. Sherburne, S. Li, M. Asta, N. Mathews, S. G. Mhaisalkar, *J. Mater. Chem. A* **2015**, *3*, 23829.
[5] Q. Chen, L. Chen, F. Ye, T. Zhao, F. Tang, A. Rajagopal, Z. Jiang, S. Jiang, A. K.-Y. Jen, Y. Xie, J. Cai, L. Chen, *Nano Lett.* **2017**, *17*, 3231.
[6] S. Öz, J.-C. Hebig, E. Jung, T. Singh, A. Lepcha, S. Olthof, F. Jan, Y. Gao, R. German, P. H. M. van Loosdrecht, K. Meerholz, T. Kirchartz, S. Mathur, *Sol. Energy Mater. Sol. Cells* **2016**, *158*, 195.
[7] B. Saparov, F. Hong, J.-P. Sun, H.-S. Duan, W. Meng, S. Cameron, I. G. Hill, Y. Yan, D. B. Mitzi, *Chem. Mater.* **2015**, *27*, 5622.
[8] D. Cortecchia, H. A. Dewi, J. Yin, A. Bruno, S. Chen, T. Baikie, P. P. Boix, M. Grätzel, S. Mhaisalkar, C. Soci, N. Mathews, *Inorg. Chem.* **2016**, *55*, 1044.
[9] Z. Yang, A. Rajagopal, C.-C. Chueh, S. B. Jo, B. Liu, T. Zhao, A. K.-Y. Jen, *Adv. Mater.* **2016**, *28*, 8990.
[10] F. Hao, C. C. Stoumpos, Z. Liu, R. P. H. Chang, M. G. Kanatzidis, *J. Am. Chem. Soc.* **2014**, *136*, 16411.
[11] N. K. Noel, S. D. Stranks, A. Abate, C. Wehrenfennig, S. Guarnera, A. Haghighirad, A. Sadhanal, G. E. Eperon, S. K. Pathak, M. B. Johnston, A. Petrozza, L. Herza, H. Snaith, *Energy EnvironSci* **2014**, *7*, 3061.
[12] F. Hao, C. C. Stoumpos, D. H. Cao, R. P. H. Chang, M. G. Kanatzidis, *Nat. Photonics* **2014**, *8*, 489.
[13] B.-B. Yu, Z. Chen, Y. Zhu, Y. Wang, B. Han, G. Chen, X. Zhang, Z. Du, Z. He, *Adv. Mater.* **2021**, *33*, 2102055.
[14] Z. Zhu, X. Jiang, D. Yu, N. Yu, Z. Ning, Q. Mi, *ACS Energy Lett.* **2022**, *7*, 2079.
[15] X. Jiang, F. Wang, Q. Wei, H. Li, Y. Shang, W. Zhou, C. Wang, P. Cheng, Q. Chen, L. Chen, Z. Ning, *Nat. Commun.* **2020**, *11*, 1245.
[16] H. Yao, T. Wu, C. Wu, L. Ding, Y. Hua, F. Hao, *Adv. Funct. Mater.* **2023**, *34*, 2312287.
[17] P. Jiang, D. Acharya, G. Volonakis, M. Zacharias, M. Kepenekian, L. Pedesseau, C. Katan, J. Even, *APL Mater.* **2022**, *10*, 060902.
[18] F. Cao, X. Xu, D. Yu, H. Zeng, *Nanophotonics* **2021**, *10*, 2221.
[19] G. Zhang, S. Xing, X. Cao, B. Zhao, D. Di, *Nanoscale* **2023**, *15*, 6954.
[20] F. Liu, R. Wu, Y. Zeng, J. Wei, H. Li, L. Manna, A. D. Mohite, *Nanoscale* **2022**, *14*, 6743.
[21] C. Pareja-Rivera, D. Morett, D. Barreiro-Argüelles, P. Olalde-Velasco, D. Solis-Ibarra, *J. Phys. Energy* **2021**, *3*, 032014.
[22] S. Kahmann, O. Nazarenko, S. Shao, O. Hordiichuk, M. Kepenekian, J. Even, M. V. Kovalenko, G. R. Blake, M. A. Loi, *ACS Energy Lett.* **2020**, *5*, 2512.
[23] M. C. Weidman, M. Seitz, S. D. Stranks, W. A. Tisdale, *ACS Nano* **2016**, *10*, 7830.
[24] D. N. Dirin, A. Vivani, M. Zacharias, T. V. Sekh, I. Cherniukh, S. Yakunin, F. Bertolotti, M. Aebli, R. D. Schaller, A. Wieczorek, S. Siol, C. Cancellieri, L. P. H. Jeurgens, N. Masciocchi, A. Guagliardi, L. Pedesseau, J. Even, M. V. Kovalenko, M. I. Bodnarchuk, *Nano Lett.* **2023**, *23*, 1914.
[25] H. Xu, H. Yuan, J. Duan, Y. Zhao, Z. Jiao, Q. Tang, *Electrochim. Acta* **2018**, *282*, 807.
[26] L. Dai, Z. Deng, F. Auras, H. Goodwin, Z. Zhang, J. C. Walmsley, P. D. Bristowe, F. Deschler, N. C. Greenham, *Nat. Photonics* **2021**, *15*, 696.
[27] M. Aminzare, J. Jiang, G. A. Mandl, S. Mahshid, J. A. Capobianco, N.-M. Dorval Courchesne, *Nanoscale* **2023**, *15*, 2997.
[28] A. Lang, I. Polishchuk, E. Seknazi, J. Feldmann, A. Katsman, B. Pokroy, *Adv. Funct. Mater.* **2020**, *30*, 2005136.
[29] Y. Takahashi, H. Hasegawa, Y. Takahashi, T. Inabe, *J. Solid State Chem.* **2013**, *205*, 39.
[30] X. Liu, Y. Wang, F. Xie, X. Yang, L. Han, *ACS Energy Lett.* **2018**, *3*, 1116.
[31] Z. Zhu, Q. Mi, *Cell Rep. Phys. Sci.* **2022**, *3*, 100690.
[32] B. Wang, H. Li, Q. Dai, M. Zhang, Z. Zou, J. Brédas, Z. Lin, *Angew. Chem.* **2021**, *133*, 17805.
[33] H. J. Lee, A. C. Jamison, T. R. Lee, *Acc. Chem. Res.* **2015**, *48*, 3007.
[34] L. Canil, T. Cramer, B. Fraboni, D. Ricciarelli, D. Meggiolaro, A. Singh, M. Liu, M. Rusu, C. M. Wolff, N. Phung, Q. Wang, D. Neher, T. Unold, P. Vivo, A. Gagliardi, F. De Angelis, *Energy Environ. Sci.* **2021**, *14*, 1429.
[35] S. Shao, J. Liu, G. Portale, H. Fang, G. R. Blake, G. H. Ten Brink, L. J. A. Koster, M. A. Loi, *Adv. Energy Mater.* **2018**, *8*, 1702019.
[36] E. W.-G. Diau, M. R., *ACS Appl. Mater. Interfaces* **2020**, *12*, 21739.
[37] Y. Numata, Y. Sanehira, R. Ishikawa, H. Shirai, T. Miyasaka, *ACS Appl. Mater. Interfaces* **2018**, *10*, 42363.
[38] J. Liu, J. Shi, D. Li, F. Zhang, X. Li, Y. Xiao, S. Wang, *Synth. Met.* **2016**, *215*, 56.
[39] S. Yang, W. Liu, L. Zuo, X. Zhang, T. Ye, J. Chen, C.-Z. Li, G. Wu, H. Chen, *J. Mater. Chem. A* **2016**, *4*, 9430.
[40] A. Halder, R. Chulliyil, A. S. Subbiah, T. Khan, S. Chattoraj, A. Chowdhury, S. K. P Sarkar, *J. Phys. Chem. Lett.* **2015**, *6*, 3483.
[41] Q. Jiang, D. Rebollar, J. Gong, E. L. Piacentino, C. Zheng, T. Xu, *Angew. Chem., Int. Ed.* **2015**, *54*, 7617.
[42] S. Karoui, H. Chouaib, S. S. Kamoun, *J. Mol. Struct.* **2022**, *1253*, 132206.
[43] P. Li, H. Dong, J. Xu, J. Chen, X. H. BoJiao, J. Li, Z. Wu, *ACS Energy Lett.* **2020**, *5*, 2327.
[44] G. Li, J. Huang, H. Zhu, Y. Li, J.-X. Tang, Y. Jiang, *Chem. Mater.* **2018**, *30*, 6099.
[45] W. Liao, D. Zhao, Y. Yu, C. R. Grice, C. Wang, A. J. Cimaroli, P. Schulz, W. Meng, K. Zhu, R. Xiong, Y. Yan, *Adv.Mater* **2016**, *28*, 9333.
[46] T.-B. Song, T. Yokoyama, J. Logsdon, M. R. Wasielewski, S. Aramaki, M. G. Kanatzidis, *ACS Appl. Energy Mater.* **2018**, *1*, 4221.
[47] S. J. Lee, S. S. Shin, Y. C. Kim, D. Kim, T. K. Ahn, J. H. Noh, J. Seo, S. I. Seok, *J. Am. Chem. Soc.* **2016**, *138*, 3974.
[48] B.o Li, H. Di, B. Chang, R. Yin, L. Fu, Y. a-N. Zhang, L. Yin, *Adv. Funct. Mater.* **2021**, *31*, 2007447.
[49] X. Liu, T. Wu, J.-Y. Chen, X. Meng, X. He, T. Noda, H. Chen, X. Yang, H. Segawa, Y. Wang, L. Han, *Energy Environ. Sci.* **2020**, *13*, 2896.
[50] X. Meng, T. Wu, X. Liu, X. He, T. Noda, Y. Wang, H. Segawa, L. Han, *J. Phys. Chem. Lett.* **2020**, *11*, 2965.
[51] H. Jang, H. Y. Lim, Y. J. Yoon, J. Seo, C. B. Park, J. G. Son, J. W. Kim, Y. S. Shin, N. G. An, S. J. Choi, S. H. Kim, J. Jeong, Y. Jo, S. K. Kwak, D. S. Kim, J. Y. Kim, *Sol. RRL* **2022**, *6*, 2200789.
[52] A. M. Boehm, T. Liu, S. M. Park, A. Abtahi, K. R. Graham, *ACS Appl. Mater. Interfaces* **2020**, *12*, 5209.
[53] Y. Zheng, Z. Fang, M. Shang, Q. Sun, J. Zheng, Z. Yang, X. Hou, W. Yang, *ACS Energy Lett.* **2021**, *6*, 2328.
[54] B. Traoré, P. Basera, A. J. Ramadan, H. J. Snaith, C. Katan, J. Even, *ACS Energy Lett.* **2022**, *7*, 349.
[55] P. Basera, B. Traoré, J. Even, C. Katan, *Nanoscale* **2023**, *15*, 11884.
[56] M. Klin, J. Nieszporek, D. Sieńko, D. Gugała-Fekner, J. Saba, *Croat. Chem. Acta* **2011**, *84*, 475.
[57] M. N., J. Prabakar, *J. Theor. Comput. Sci.* **2015**, *2*, 1000137.
[58] E. J. C. Lien, W. D. Kumler, *J. Med. Chem.* **1968**, *11*, 214.
[59] L. S. Rao, B. K. Gupta, CNDO Calculations of Some Thioamides–Hl.
[60] H. Kim, R. Keller, W. D. Gwinn, *J. Chem. Phys.* **1962**, *37*, 2748.
[61] J. R. Durig, C. Zheng, H. Deeb, *J. Mol. Struct.* **2006**, *784*, 78.
[62] Y. Zhang, M. Chen, T. He, H. Chen, Z. Zhang, H. Wang, H. Lu, Q. Ling, Z. Hu, Y. Liu, Y. Chen, G. Long, *Adv. Mater.* **2023**, *35*, 2210836.
[63] M. Melosso, A. Melli, L. Spada, Y. Zheng, J. Chen, M. Li, T. Lu, G. Feng, Q. Gou, L. Dore, V. Barone, C. Puzzarini, *J. Phys. Chem. A* **2020**, *124*, 1372.
[64] Z. Li, J. Ji, C. Zhang, Q. Hou, P. Jin, *J. Phys. Chem. C* **2020**, *124*, 14147.

[65] L. Pedesseau, D. Sapori, B. Traore, R. Robles, H.-H. Fang, M. A. Loi, H. Tsai, W. Nie, J.-C. Blancon, A. Neukirch, S. Tretiak, A. D. Mohite, C. Katan, J. Even, M. Kepenekian, *ACS Nano* **2016**, *10*, 9776.
[66] J. L. Knutson, J. D. Martin, D. B. Mitzi, *Inorg. Chem.* **2005**, *44*, 4699.
[67] J. Even, L. Pedesseau, J.-M. Jancu, C. Katan, *J. Phys. Chem. Lett.* **2013**, *4*, 2999.
[68] N. Alhazmi, E. Pineda, J. Rawle, J. R. Howse, A. D. F. Dunbar, *ACS Appl. Energy Mater.* **2020**, *3*, 6155.
[69] S. Lilliu, J. Griffin, A. T. Barrows, M. Alsari, B. Curzadd, T. G. Dane, O. Bikondoa, J. E. Macdonald, D. G. Lidzey, *CrystEngComm* **2016**, *18*, 5448.
[70] T. Yamamoto, I. W. H. Oswald, C. N. Savory, T. Ohmi, A. A. Koegel, D. O. Scanlon, H. Kageyama, J. R. Neilson, *Inorg. Chem.* **2020**, *59*, 17379.
[71] S. Wu, L. Meng, Z. Zhang, M. Li, Y. Yang, J. Wang, H. Chen, C. Jiang, X. Wan, C. Li, Z. Yao, Y. Chen, *J. Mater. Chem. C* **2022**, *10*, 1977.
[72] F. Zhang, D. H. Kim, H. Lu, J.-S. Park, B. W. Larson, J. Hu, L. Gao, C. Xiao, O. G. Reid, X. Chen, Q. Zhao, P. F. Ndione, J. J. Berry, W. You, A. Walsh, M. C. Beard, K. Zhu, *J. Am. Chem. Soc.* **2019**, *141*, 5972.
[73] R. Alkarsifi, T. Buffeteau, C. Labrugère-Sarroste, L. Hirsch, D. M. Bassani, T. Toupance, *J. Mater. Chem. C* **2023**, *11*, 16056.
[74] J. Byeon, S. H. Cho, J. Jiang, J. Jang, C. Katan, J. Even, J. Xi, M. Choi, Y. S. Lee, *ACS Appl. Mater. Interfaces* **2023**, *15*, 27853.
[75] M. Shao, T. Bie, L. Yang, Y. Gao, X. Jin, F. He, N. Zheng, Y. Yu, X. Zhang, *Adv. Mater.* **2022**, *34*, 2107211.
[76] D. Thrithamarassery Gangadharan, D. Valverde-Chávez, A.-F. Castro-Méndez, V. Prakash, R. Izquierdo, C. Silva, D. Ma, J.-P. Correa-Baena, *ACS Appl. Energy Mater.* **2021**, *4*, 2616.
[77] M. Liao, B. Yu, Z. Jin, W. Chen, Y. Zhu, X. Zhang, W. Yao, T. Duan, I. Djerdj, *ChemSusChem* **2019**, *12*, 5007.
[78] T. Liu, R. A. Scheidt, X. Zheng, S. Joy, Q. Jiang, H. R. Atapattu, M. Chen, H. Pruett, K. Zhu, J. M. Luther, M. C. Beard, K. R. Graham, *Cell Rep. Phys. Sci.* **2023**, *4*, 101650.
[79] Q. Chen, J. Luo, R. He, H. Lai, S. Ren, Y. Jiang, Z. Wan, W. Wang, X. Hao, Y. Wang, J. Zhang, I. Constantinou, C. Wang, L. Wu, F. Fu, D. Zhao, *Adv. Energy Mater.* **2021**, *11*, 2101045.
[80] S. Gupta, T. Bendikov, G. Hodes, D. Cahen, *ACS Energy Lett.* **2016**, *1*, 1028.
[81] S. Gupta, G. Hodes, *SN Appl. Sci.* **2019**, *1*, 1066.
[82] R. Nishikubo, N. Ishida, Y. Katsuki, A. Wakamiya, A. Saeki, *J. Phys. Chem. C* **2017**, *121*, 19650.
[83] F. Giustino, A. Pasquarello, *Phys. Rev. B* **2005**, *71*, 144104.
[84] N. Shi, R. Ramprasad, *Phys. Rev. B* **2006**, *74*, 045318.
[85] D. Sapori, M. Kepenekian, L. Pedesseau, C. Katan, J. Even, *Nanoscale* **2016**, *8*, 6369.
[86] J. Lahnsteiner, R. Jinnouchi, M. Bokdam, *Phys. Rev. B* **2019**, *100*, 094106.
[87] B. Traore, L. Pedesseau, L. Assam, X. Che, J.-C. Blancon, H. Tsai, W. Nie, C. C. Stoumpos, M. G. Kanatzidis, S. Tretiak, A. D. Mohite, J. Even, M. Kepenekian, C. Katan, *ACS Nano* **2018**, *12*, 3321.
[88] O. N. Oliveira, D. M. Taylor, T. J. Lewis, S. Salvagno, C. J. M. Stirling, *J. Chem. Soc. Faraday Trans. 1 Phys. Chem. Condens. Phases* **1989**, *85*, 1009.
[89] J. T. Davies, S. E. I. P. Rideal, *Can. J. Chem.* **1955**, *33*, 947.
[90] P. C. Rusu, G. Brocks, *J. Phys. Chem. B* **2006**, *110*, 22628.
[91] C. Goh, S. R. Scully, M. D. McGehee, *J. Appl. Phys.* **2007**, *101*, 114503.
[92] E. Artacho, E. Anglada, O. Diéguez, J. D. Gale, A. García, J. Junquera, R. M. Martin, P. Ordejón, J. M. Pruneda, D. Sánchez-Portal, J. M. T. S. M. Soler, *J. Phys. Condens. Matter* **2008**, *20*, 064208.
[93] J. M. Soler, E. Artacho, J. D. Gale, A. García, J. Junquera, P. Ordejón, *J. Phys. Condens. Matter* **2002**, *14*, 2745.
[94] V. R. V. D. Cooper, *Phys. Rev. B* **2010**, *81*, 161104.
[95] I. Hamada, M. Otani, *Phys. Rev. B* **2010**, *82*, 153412.
[96] E. Bitzek, P. Koskinen, F. Gähler, M. Moseler, P. Gumbsch, *Phys. Rev. Lett.* **2006**, *97*, 170201.
[97] J. P. Perdew, K. Burke, M. Ernzerhof, *Phys. Rev. Lett.* **1996**, *77*, 3865.
[98] L. Fernández-Seivane, M. A. Oliveira, S. Sanvito, J. Ferrer, *J. Phys. Condens. Matter* **2006**, *18*, 7999.
[99] S. García-Gil, A. García, N. Lorente, P. Ordejón, *Phys. Rev. B* **2009**, *79*, 075441.
[100] T. C. Leung, C. L. Kao, W. S. Su, Y. J. Feng, C. T. Chan, *Phys. Rev. B* **2003**, *68*, 195408.
[101] A. Franciosi, *Surf. Sci. Rep.* **1996**, *25*, 1.
[102] E. C. Schueller, G. Laurita, D. H. Fabini, C. C. Stoumpos, M. G. Kanatzidis, R. Seshadri, *Inorg. Chem.* **2018**, *57*, 695.
[103] L. Lanzetta, T. Webb, N. Zibouche, X. Liang, D. Ding, G. Min, R. J. E. Westbrook, B. Gaggio, T. J. Macdonald, M. S. Islam, S. A. Haque, *Nat. Commun.* **2021**, *12*, 2853.